
Article:
Yu, J., Yong, X. orcid.org/0000-0003-1674-754X and Lu, S. orcid.org/0000-0003-4538-7846 (2024) p-d orbital hybridization engineered single-atom catalyst for electrocatalytic ammonia synthesis. Energy & Environmental Materials, 7 (2). e12587. ISSN 2575-0356

https://doi.org/10.1002/eem2.12587

RESEARCH ARTICLE

Nitrogen Reduction

Energy & Environmental Materials WILEY

p-d Orbital Hybridization Engineered Single-Atom Catalyst for Electrocatalytic Ammonia Synthesis

Jingkun Yu, Xue Yong, and Siyu Lu**

The rational design of metal single-atom catalysts (SACs) for electrochemical nitrogen reduction reaction (NRR) is challenging. Two-dimensional metal–organic frameworks (2DMOFs) is a unique class of promising SACs. Up to now, the roles of individual metals, coordination atoms, and their synergy effect on the electroanalytic performance remain unclear. Therefore, in this work, a series of 2DMOFs with different metals and coordinating atoms are systematically investigated as electrocatalysts for ammonia synthesis using density functional theory calculations. For a specific metal, a proper metal-intermediate atoms p-d orbital hybridization interaction strength is found to be a key indicator for their NRR catalytic activities. The hybridization interaction strength can be quantitatively described with the p−/d- band center energy difference (Δd-p), which is found to be a sufficient descriptor for both the p-d hybridization strength and the NRR performance. The maximum free energy change (ΔG_{max}) and Δd-p have a volcanic relationship with $OsC_4(Se)_4$ located at the apex of the volcanic curve, showing the best NRR performance. The asymmetrical coordination environment could regulate the band structure subtly in terms of band overlap and positions. This work may shed new light on the application of orbital engineering in electrocatalytic NRR activity and especially promotes the rational design for SACs.

1. Introduction

Ammonia, an important chemical raw material, plays an important role in the fields of industry, agriculture production, energy storage, and conversion.[1,2] At present, ammonia mainly comes from the traditional Haber-Bosch ammonia synthesis process, which operates under harsh conditions, i.e., high temperature (300–500 °C) and high pressure (150–300 atm).[3,4] This process requires a lot of energy input, but the conversion rates and yields are quite low and results in serious environmental pollution problems. The electrochemical ammonia synthesis ($N_2 \rightarrow NH_3$) method has become an attractive alternative process of Harber-Bosch, due to the renewable electricity input, such as solar cells and operates at room temperature and pressure.[5–7] Electrochemical techniques can activate the adsorbed N_2 molecules on the catalyst by donating electrons, while thermodynamic equilibrium has almost no limit on the conversion rate.

Due to the extremely high stability of the nonpolar N≡N (941 kJ mol^{-1}) triple bond in N_2, an efficient and inexpensive catalyst with high selectivity is required to reduce energy consumption. Single-atom catalysts (SACs) have attracted wide interest in the field of electrocatalysis because of their high atom utilization efficiency.[8–11] Metal atoms can be distributed in the substrate independently and regularly, which can not only reduce the metal loading and improve the utilization efficiency of metal atoms but also change the adsorption and desorption selectivity of the active components on the catalyst to different molecules, thereby affecting the kinetics of the reaction. In addition, the simplified SACs system is more conducive to exploring the path of the reaction mechanisms and provides excellent guidance for the design of better catalysts.

Two-dimensional metal–organic frameworks (2DMOFs) with metals and organic ligands form a unique class of SACs. Most 2DMOFs have high specific surface areas and excellent electrical conductivity, which are beneficial for electron transfer in the electrocatalytic process.[12–15] In recent years, several 2DMOFs have been applied as electrocatalysts for CO_2 reduction, water splitting, and nitrogen reduction reactions (NRR) in both theoretical and experimental work.[16–20] Kambe et al. synthesized a two-dimensional planar MOFs (π-conjugated metal bis[dithiolene] complex [MC_4S_4]) material for the first time and demonstrated its high electrical conductivity.[21] Afterward, researchers conducted extensive research on it. For example, NiC_4S_4 nanosheet has high electrical conductivity and catalytic activity in detecting toxic CO, and it can bind and release ethylene molecules under neutral and reducing conditions;[22] IrC_4S_4 shows high catalytic activity for oxygen reduction and methanol resistance;[23] while CoC_4S_4 has been proven to be an efficient electrocatalyst for hydrogen evolution from water.[24] Recently, Liu et al. proved that different metal active centers have different adsorption energy for N_2, and metal Os has moderate adsorption energy for N_2, leading to the minimum reaction overpotential.[25] However, the role of individual metals, coordination atoms, and their synergy effect on the electroanalytic performance are not clear, which further hinders the systematic engineering of efficient NRR SACs. Therefore, a comprehensive theoretical study of this issue will facilitate the further development of novel NRR catalysts and provide useful guidance for promoting sustainable NH_3 production.

Dr. J. Yu, Prof. S. Lu
Green Catalysis Center, and College of Chemistry, Zhengzhou University, Zhengzhou 450001, China
E-mail: sylu2013@zzu.edu.cn
Prof. X. Yong
Department of Chemistry, University of Sheffield, SheffieldS37HF, UK
E-mail: x.yong@sheffield.ac.uk
The ORCID identification number(s) for the author(s) of this article can be found under https://doi.org/10.1002/eem2.12587.

DOI: 10.1002/eem2.12587

To this end, we systematically investigated a series of 2DMOFs including MC_4X_4 (M=Os, Ru, Ir; X=O, S, Se, NH, **Figure 1a**) as electrocatalysts for NRR based on density functional theory (DFT) calculations. The results show that for good NRR catalytic activities, the p-d hybridization interactions between the metals and adsorbate atoms should be neither too strong nor too weak, which further affects the adsorption performance of reaction intermediates. For a specific type of metal, both the p-d hybridization strength and the NRR performance are found to be determined by the p-/d- band center energy difference (Δd-p). The maximum free energy change (ΔG_{max}) of the NRR and Δd-p have a volcanic relationship, $OsC_4(Se)_4$, IrC_4O_4, and $RuC_4(Se)_4$ are located at the apex of the volcano diagrams. Furthermore, $OsC_4(Se)_4$, IrC_4O_4, and $RuC_4(Se)_4$ are nitrogen-free, which can effectively prevent the catalyst from decomposing to form NH_3.[26] They all have a great degree of inhibitory effect on the competing reaction of hydrogen evolution (HER), making them with high NRR selectivity. Our results systematically proved the application of orbital engineering in electrocatalytic NRR activity, paving the way for the design of a new type of SACs for NRR.

2. Results and Discussion

2.1. Stabilities of MC_4X_4

The optimized structures of MC_4X_4 are all planar (Figure S1, Supporting Information). Their stabilities were evaluated by the formation energies (E_{form}) which were calculated by the following formula:

$$E_{form} = E_{M_3(C_6X_6)_2} - 2E_{C_6X_6H_6} - 3E_{M-bulk}/N + 12E_H \quad (1)$$

where $E_{M_3(C_6X_6)_2}$, $E_{C_6X_6H_6}$, and E_{M-bulk} were the total energies of $M_3(C_6X_6)_2$, $C_6X_6H_6$, and metal bulk, respectively, N represented the number of metal atoms in the bulk.[27] A more negative E_{form} corresponds to higher stability of the catalyst. A stable $M_3(C_6X_6)_2$ structure should satisfy the criterion $E_{form} < 0$. Tables S1–S3, Supporting Information, show the formation energies of $M_3(C_6X_6)_2$, and the E_{form} values are in the range from −3.56 to −10.59 eV. Such negative values of E_{form} strongly attest that the good structural stability of the established $M_3(C_6X_6)_2$ model. We then calculated their phonon spectra to explore the dynamic stability of metal Os as a representative. The phonon spectrum results of OsC_4X_4 are shown in Figure S2, Supporting Information. All systems have no imaginary frequency, which further confirms their stability.

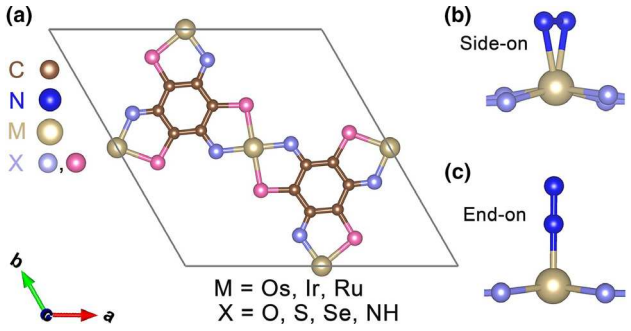

Figure 1. a) Structures of MC_4X_4 (M = Ru, Os, Ir; X = O, S, Se, NH) and two represent adsorption modes of $*N_2$ on metal site of MC_4X_4: b) side-on; c) end-on.

2.2. N_2 Adsorption on MC_4X_4

The first step of NRR is the chemisorption and activation of the N_2 molecule by the catalytic active center, which activate the N≡N bond.[28,29] Therefore, we first calculated the N_2 adsorption energy on MC_4X_4 based on:

$$E_{ads} = E_{MC_4X_4-N_2} - (E_{N_2} + E_{MC_4X_4}) \quad (2)$$

where E_{N_2}, $E_{MC_4X_4}$, and $E_{MC_4X_4-N_2}$ are the total energies of an isolated N_2 molecule, MC_4X_4 nanosheet, and the adsorbed system, respectively. According to these definitions, a negative E_{ads} value indicates an exothermic adsorption process.

The adsorption of N_2 can be both dissociative and associative (Figure 3a). However, dissociative absorption requires very high energy barriers (from 4.93 to 5.74 eV for OsC_4X_4) (Figure S3, Supporting Information) as compared with associative absorption (see below for details). This is because the scission of N≡N requires a high kinetic barrier which makes the dissociative adsorption of N_2 under milder conditions unfavorable.[30] Consequently, only the associative path is considered as the main mechanism of the reaction.

For associative absorption, the N_2 molecule can be adsorbed on MC_4X_4 in two modes: side-on and end-on (Figure 1b,c). In the side-on mode, N_2 is absorbed parallelly to the MC_4X_4 nanosheet forming two chemical bonds with the transition metal atom. While in the end-on mode, N_2 is vertically absorbed on the transition metal atom. For the end-on adsorption configuration, OsC_4X_4 has negative N_2 adsorption energies (E_{ads}: from −0.02 to −1.62 eV) (Table S4, Supporting Information); for the side-on adsorption configuration, the N_2 adsorption energies on OsC_4X_4 are relatively weaker than in the end-on adsorption configuration (**Figure 2a**). For IrC_4X_4 and RuC_4X_4, end-on adsorption configurations also have more negative adsorption energies (Tables S5 and S6, Supporting Information). The comparison results reveal that N_2 molecules prefer to be absorbed as the end-on configuration.

According to the Sabatier principle, the ideal NRR catalysts should have moderate adsorption energy for different intermediates (N_2, NNH, NH, NH_2, and NH_3, etc.), which should not be too strong or too weak. This indicates that the excessive adsorption energy of N_2 on $OsC_4(NH)_4$ may have a negative impact on the entire NRR process. The N≡N triple bond lengths of the absorbed N_2 on OsC_4O_4 (1.13 Å), OsC_4S_4 (1.14 Å), $OsC_4(Se)_4$ (1.14 Å), and $OsC_4(NH)_4$ (1.14 Å) become larger than that (1.10 Å) of an isolated N_2 molecule; for the asymmetrical structures, the N≡N triple bond lengths are all approximately 1.14 Å (Figure S4, Supporting Information). These results indicate that the triple bond of the N_2 molecule is activated. The distances between Os and adsorbed N atoms are also related to different coordinating atoms: $OsC_4(NH)_4$ has the shortest Os=N bond (1.82 Å), while the others have longer Os=N bond length (from 1.84 to 1.89 Å), which corresponds to the strength of the adsorption energy.

In order to have a deeper understanding of the effect of different coordination atoms on the absorption N_2 adsorption on nanosheet, we calculated the charge density difference and Bader charge of

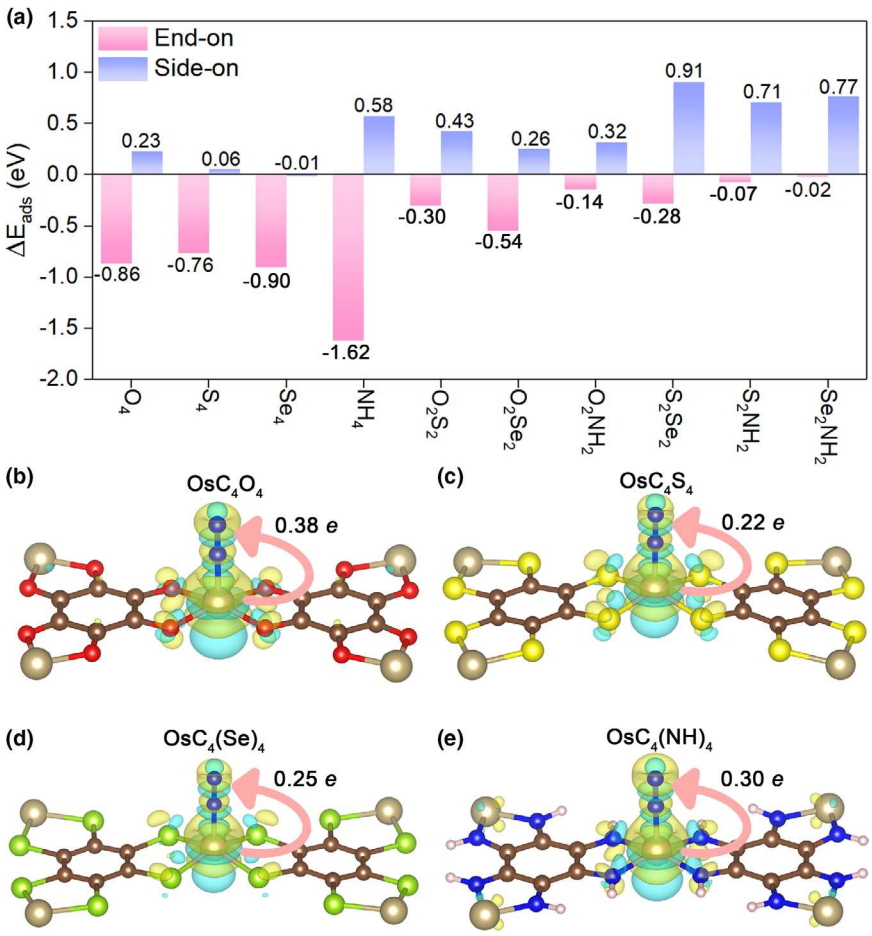

Figure 2. a) The computed adsorption energies of N_2 molecule on OsC_4X_4 nanosheet; the charge density difference, as well as Bader charge analysis at of $*N_2$ on b) OsC_4O_4, c) OsC_4S_4, d) $OsC_4(Se)_4$, and e) $OsC_4(NH)_4$. Charge accumulation and depletion are illustrated by yellow and blue regions with the isosurface of 0.002 $eÅ^{-3}$.

adsorbed N_2 molecule (Figure 2b–e). The absorbed N_2 are polarized with nonsymmetrical charge density distributions. The charge density difference results also show that all catalysts have positive and negative charges around the Os atoms, indicating a clear electron transfer between Os and N_2. The charge transfer between N_2 and OsC_4X_4 mainly follow the electron "accept-donation" mechanism. The empty d orbital of the Os atom can accept the lone pair electrons of N_2, while the antibonding state of N_2 can accept electrons from the d orbital of the Os atom, activating the N≡N bond. Bader charge analysis showed that Os atoms of OsC_4O_4, OsC_4S_4, $OsC_4(Se)_4$, and $OsC_4(NH)_4$ lost 1.63, 0.86, 0.60, and 1.20 electrons, respectively, while the N atoms connected to the Os active center gained 0.41, 0.38, 0.42, and 0.35 electrons, respectively, these results fully demonstrate the effect of different coordination atoms on the charge transfer of N_2 adsorption.

2.3. Electrochemical Catalytic Activity of OsC_4X_4 for the NRR

We then used the side-on absorption configuration for intermediates involved in the six protons and electrons transfer process in NRR ($N_2 + 6H^+ + 6e^- = 2NH_3$). The potential determination steps (PDS) are determined as the most energetic step. The overpotential (η) of the whole NRR is computed based on:

$$\eta = U_e - U_L \tag{3}$$

where U_e is the equilibrium potential ($U_e = -0.18$ V for NRR) and U_L is the limiting potential, defined as the minimum applied potential to make the PDS occur spontaneously:

$$U_L = \frac{-\Delta G_{max}}{e} \tag{4}$$

We considered both distal and alternating reaction pathways for the hydrogenation process of NRR (**Figure 3a**).[31] In the distal path, the first distal N atom reacts with three consecutive ($H^+ + e^-$) pairs to generate one ammonia molecule and leave the catalyst surface. The remaining N atom then continues to be hydrogenated to produce another NH_3 molecule. In the alternating path, the two N atoms of absorbed N_2 on the catalyst surface are alternately hydrogenated, and the second NH_3 molecule is released immediately following the release of the first NH_3 molecule.

The reaction free energy diagrams of the NRR process on OsC_4O_4, OsC_4S_4, $OsC_4(Se)_4$, and $OsC_4(NH)_4$ nanosheets are displayed in Figure 3b–e. In the first ($H^+ + e^-$) transferring step, the adsorbed N_2 is hydrogenated to $*N_2H$, where H binds to the N at the far end. After the formation of $*N_2H$ species, the N–N bond is further elongated to 1.22, 1.21, 1.22, and 1.18 Å on OsC_4O_4, OsC_4S_4, $OsC_4(Se)_4$, and $OsC_4(NH)_4$, respectively. The N orbital hybridization has changed from sp to sp^2 which requires a reaction barrier of 0.70 eV for OsC_4O_4, 0.55 eV for OsC_4S_4, 0.53 eV for $OsC_4(Se)_4$, and 1.77 eV for $OsC_4(NH)_4$, respectively. For the asymmetrical structures, the N–N bond is elongated to 1.22, 1.21, 1.23, 1.21, 1.22, and 1.22 Å for $OsC_4O_2S_2$, $OsC_4O_2Se_2$, $OsC_4O_2(NH)_2$, $OsC_4S_2Se_2$, $OsC_4S_2(NH)_2$, and $OsC_4Se_2(NH)_2$. The energy barriers of $*N_2 + H^+ + e^- \rightarrow *N_2H$ step are 0.59, 0.61, 0.79, 0.58, 0.65, and 0.62 eV respectively (Figure S5, Supporting Information). This indicates that the formation of $*N_2H$ is a nonspontaneous process. This step is thus also identified as the rate-determined step with the highest reaction barrier for all the NRR reactions on OsC_4O_4, OsC_4S_4, $OsC_4(Se)_4$, $OsC_4O_2S_2$, $OsC_4O_2Se_2$, $OsC_4O_2(NH)_2$, $OsC_4S_2Se_2$, $OsC_4S_2(NH)_2$, and $OsC_4Se_2(NH)_2$ catalysts.

The $*N_2H$ intermediate is further hydrogenated with the second pair of H^+/e^- forming two different $*N_2H_2$ species: $*NNH_2$ (distal hydrogenation pathway) and *NHNH (alternate hydrogenation pathway). In the distal hydrogenation reaction pathway, the formation of $*NNH_2$ from $*N_2H$ on OsC_4O_4, OsC_4S_4, $OsC_4(Se)_4$, $OsC_4O_2S_2$, $OsC_4O_2Se_2$, $OsC_4S_2Se_2$ and $OsC_4S_2(NH)_2$ are all barrierless and downhill in the free energy diagram. A barrier of 0.18, 0.08, and 0.22 eV is required to

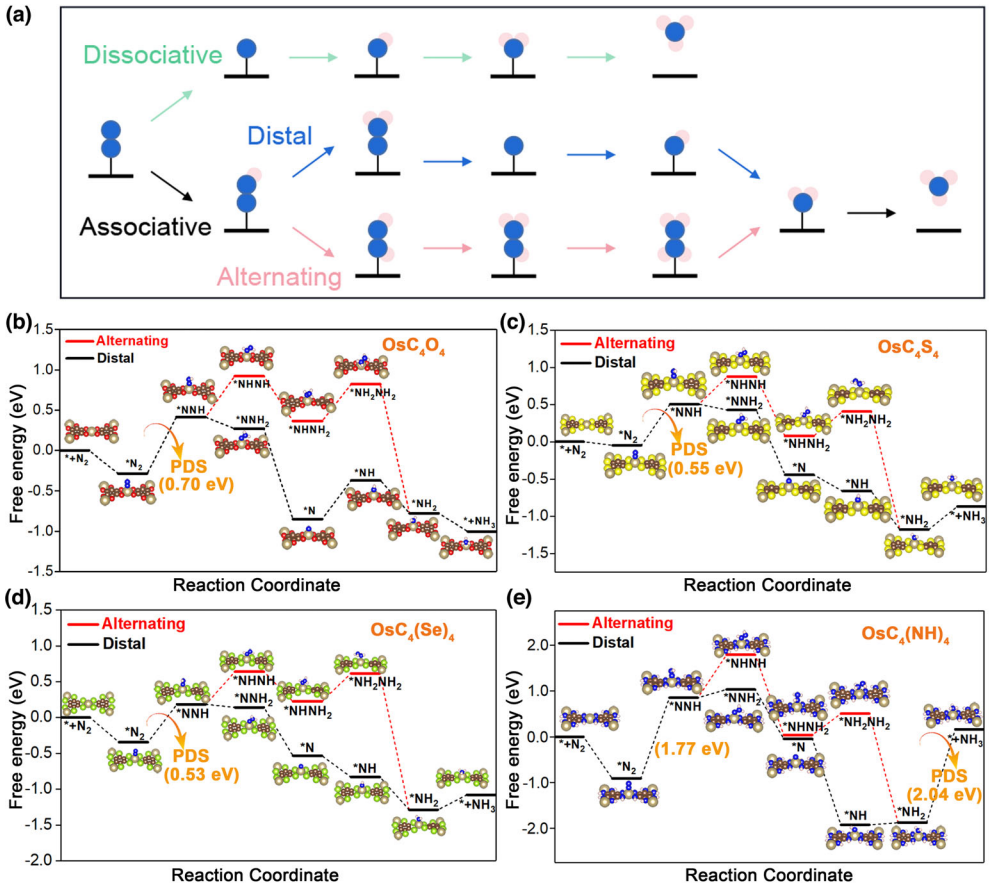

Figure 3. a) Schematic diagram for the electrochemical reduction of N_2 into NH_3 through dissociative and associative pathways; and the reaction free energy diagrams and the absorbed intermediates configurations of NRR on b) OsC_4O_4; c) OsC_4S_4; d) $OsC_4(Se)_4$; e) $OsC_4(NH)_4$. For the system studied, the N_2 was mainly associatively absorbed on the slab, then hydrogenation of $N_2 \rightarrow NH_3$ mainly underwent through distal pathway.

form $*NNH_2$ on $OsC_4(NH)_4$, $OsC_4O_2(NH)_2$, and $OsC_4Se_2(NH)_2$. Subsequently, the third pair of H^+/e^- is exothermically transferred to the $*NNH_2$ species and form the first NH_3 molecule with the release of 1.12, 0.87, 0.67, 1.08, 0.87, 0.70, 0.36, 0.82, 1.19, and 0.41 eV free energies on OsC_4O_4, OsC_4S_4, $OsC_4(Se)_4$, $OsC_4(NH)_4$, $OsC_4O_2S_2$, $OsC_4O_2Se_2$, $OsC_4O_2(NH)_2$, $OsC_4S_2Se_2$, $OsC_4S_2(NH)_2$, and $OsC_4Se_2(NH)_2$. After the first NH_3 molecule is released, the second N atom could be gradually hydrogenated to *NH, $*NH_2$ easily by accepting the fourth, and fifth pair of H^+/e^- with a downhill free energy diagram. The second NH_3 was formed after the sixth pair of H^+/e^- reacted with $*NH_2$. This step is only barrierless on OsC_4O_4 while barriers of 0.31, 0.21, 2.04, 0.06, 0.19, 0.22, 0.19, 0.17 and 0.18 eV exist for OsC_4S_4, $OsC_4(Se)_4$, $OsC_4(NH)_4$, $OsC_4O_2S_2$, $OsC_4O_2Se_2$, $OsC_4O_2(NH)_2$, $OsC_4S_2Se_2$, $OsC_4S_2(NH)_2$ and $OsC_4Se_2(NH)_2$. Overall, in the distal hydrogenation mechanism, the formation of $*N_2H$ intermediate is the PDS of the whole reaction path for OsC_4O_4, OsC_4S_4, $OsC_4(Se)_4$, $OsC_4O_2S_2$, $OsC_4O_2Se_2$, $OsC_4O_2(NH)_2$, $OsC_4S_2Se_2$, $OsC_4S_2(NH)_2$, and $OsC_4Se_2(NH)_2$, while $OsC_4(Se)_4$ has the smallest limiting potential of −0.53 eV. As for $OsC_4(NH)_4$, a larger energy barrier is required for the $*NH_2 + H^+ + e^- \rightarrow * + NH_3$ step (2.04 eV), due to its stronger adsorption of NH_3.

Compared with the distal hydrogenation path, the alternate hydrogenation pathway is not preferred because a much higher barrier (0.51, 0.37, 0.46, 0.94, 0.47, 0.43, 0.39, 0.37, 0.38 and 0.46 eV for OsC_4O_4, OsC_4S_4, $OsC_4(Se)_4$, $OsC_4(NH)_4$, $OsC_4O_2S_2$, $OsC_4O_2Se_2$, $OsC_4O_2(NH)_2$, $OsC_4S_2Se_2$, $OsC_4S_2(NH)_2$, and $OsC_4Se_2(NH)_2$) are needed for absorption of the second pair of H^+/e^- the and form *NHNH. This indicates that it is an endothermic process and could not proceed spontaneously. In addition, the generation of $*NH_2NH_2$ after absorption of the third and fourth pair of H^+/e^- also requires additional energy input and makes the alternate hydrogenation pathway less favorable. Similar to the distal hydrogenation mechanism, the formation of $*N_2H$ species is the PDS of the alternate hydrogenation pathway. However, from a thermodynamic point of view, the distal mechanism is energetically more likely to occur. The overpotential of NRR on OsC_4O_4, OsC_4S_4, $OsC_4(Se)_4$, $OsC_4(NH)_4$, $OsC_4O_2S_2$, $OsC_4O_2Se_2$, $OsC_4O_2(NH)_2$, $OsC_4S_2Se_2$, $OsC_4S_2(NH)_2$, and $OsC_4Se_2(NH)_2$ is computed to be 0.52, 0.37, 0.35, 1.86, 0.41, 0.43, 0.61, 0.40, 0.47, and 0.44 V, respectively. The overpotential of $OsC_4(Se)_4$ is comparable with that of previously reported Fe-embedded metal–organic frameworks (0.35 V).[32] Therefore, $OsC_4(Se)_4$ could serve as a promising NRR electrocatalyst.

2.4. Origin of NRR Catalytic Activity

The adsorption strength of the reaction intermediates was determined by the electronic state of the catalyst surface. In order to explore the difference in absorption strength on different nanosheets, we further studied the electronic structures of OsC_4X_4. Since the formation of $*N_2H$ is the PDS, we also analyzed the projected density of states (PDOS) of $*N_2H$ (**Figure 4**a, Figure S6, Supporting Information). Obviously, the results show that both the d orbital of the metal atom and the p orbital of -N_2H contribute to the total density of states around the Fermi level for all the systems. The metal and the intermediate (N_2H) form covalent bonds through p-d hybridization interaction. And thus, the p and d peaks in the PDOS overlap with each other near the Fermi level, while there are differences in the position of the d band center and p band center. We define the difference between d band center (E_d) and p band center (E_p) as Δd-p:

$$\Delta d\text{-}p = E_d - E_p \quad (5)$$

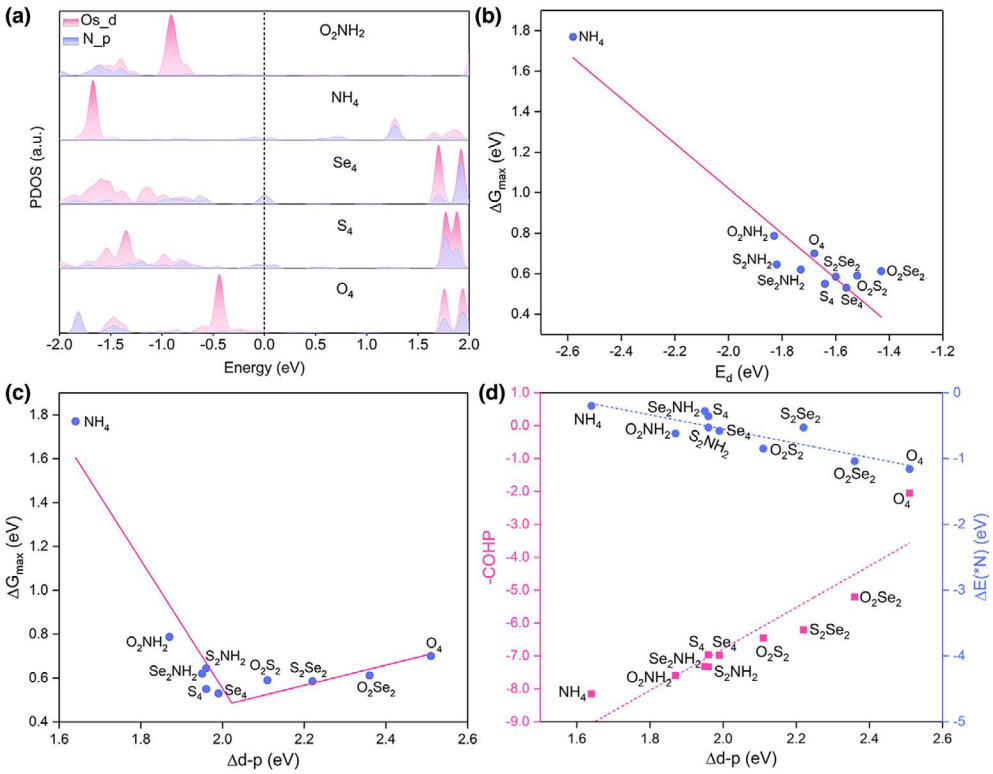

Figure 4. a) PDOS of $*N_2H$ on OsC_4O_4, OsC_4S_4, $OsC_4(Se)_4$, $OsC_4(NH)_4$, $OsC_4O_2(NH)_2$; b) the correlation between the E_d and ΔG_{max} on OsC_4X_4; c) the volcano-type curve of ΔG_{max} against the Δd-p; d) the correlation between the COHP (ΔE[*N]) and Δd-p on OsC_4X_4.

The calculated E_d of Os, E_p of N_2H and the corresponding ΔG_{max} values are shown in Table S7, Supporting Information, and the PDOS of OsC_4X_4 are shown in Figure S7, Supporting Information. The E_d shift lower in energy below the Fermi level in the order of $OsC_4(NH)_4$ (−2.58 eV) < $OsC_4O_2(NH)_2$ (−1.83 eV) < $OsC_4S_2(NH)_2$ (−1.82 eV) < $OsC_4Se_2(NH)_2$ (−1.73 eV) < OsC_4O_4 (−1.68 eV) < OsC_4S_4 (−1.64 eV) < $OsC_4S_2Se_2$ (−1.60 eV) < $OsC_4(Se)_4$ (−1.56 eV) < $OsC_4O_2S_2$ (−1.52 eV) < $OsC_4O_2Se_2$ (−1.43 eV). The S and Se have larger sizes and weaker electron affinity, thus weaker p-d hybridization in $OsC_4O_2S_2$ and $OsC_4O_2Se_2$. The distinct dz^2 levels are higher in energy level than the p-d hybridization levels. Thus, S, Se coordination atoms lead to the d band center close to the Fermi level. The p orbital (p_y) of O shows a larger overlap with dyz. The introduction of p_y also shifts dz^2 lower to the Fermi level. Thus, the overall effect makes the d band center less close to the Fermi level than those of S and Se coordination. −NH group can be both an electron donator and electron acceptor, thus it behaves slightly differently. The p-d hybridization and distinct dz^2 are at similar energy levels. Compare with O coordination atoms, the d band center of the $MC_4(NH)_4$ is lower than the d band center of OsC_4O_4. In the compounds with the asymmetrical coordination atoms, some of the d band centers are located between those with four same coordination atoms; while some are closer to Fermi than both symmetrical coordination environments. For example, the combination of $Se_2(NH)_2$ coordination forms d-p hybridization level which is below dz^2 but lies between that of $OsC_4(NH)_4$ and OsC_4Se_4. The d band center of $OsC_4Se_2(NH)_2$ is between of $OsC_4(NH)_4$ and OsC_4Se_4. The d-p hybridization of OsO_2Se_2 is similar to OsC_4O_4 but the dz^2 bands is more like that of OsC_4Se_4. Thus, the d band center of $OsC_4O_2Se_2$ shifts further close to Fermi (Figure S8, Supporting Information). These results demonstrate that the change of the coordinating atoms can successfully adjust the E_d of Os atom. In particular, the mixing of asymmetrical atoms can create subtle regulation in the band structure depending on the d-p hybridization and the dz^2 orbitals. The absorption strength of *N, *NH, $*NH_2$, $*N_2H$ was scaled well with E_d which meets the well-known d-band center theory in electrocatalyst.[33] And thus, ΔG_{max} decreases almost linearly with the increase of E_d levels toward E_f (Figure 4b). For the 4-coordinated Os ($4f^{14}5^{d6}6^{s2}$), it is the dz^2 that dominates the d band position. The dz^2 orbital can maximize the head-on orbital overlapping to form a sigma bond when interacting with N_2 and N- containing intermediates as it is perpendicular to the basal plane.[34,35] This can also explain why Os metal gives better performance. Interestingly, ΔG_{max} is found to have an obvious volcanic relationship with the Δd-p, $OsC_4(Se)_4$ is located near the apex of the volcanic curve and has the best NRR performance (Figure 4c). The Δd-p can quantitively describe the bonding strength between the metal and the intermediates. A too large or too small difference is detrimental to the NRR process. On one hand, a larger Δd-p would suggest weak orbital resonance/overlaps that result in weaker bonding but stronger adsorption of the intermediate. For example, OsC_4O_4 has a large Δd-p of 2.51 eV but a strong absorption of *N. On the other hand, a smaller Δd-p will result in weak adsorption of the intermediate by the catalyst, which will eventually lead to the deactivation of the catalyst surface. For example, $OsC_4(NH)_4$ has a Δd-p of 1.64 eV and a weak absorption of *N. Therefore, for a highly active NRR catalyst, an appropriate energy-level difference is required to balance the adsorption and desorption of intermediates. This also opens a way of engineering the metal-coordination atom bonding interaction in SACs for better the NRR electrocatalytic activity.

To characterize the metal-coordination atom interaction strength, we further computed the crystal orbital Hamilton population (COHP) (Figure S9, Supporting Information). The COHP values of OsC_4O_4, OsC_4S_4, $OsC_4(Se)_4$, $OsC_4(NH)_4$, $OsC_4O_2S_2$, $OsC_4O_2Se_2$, $OsC_4O_2(NH)_2$, $OsC_4S_2Se_2$, $OsC_4S_2(NH)_2$, and $OsC_4Se_2(NH)_2$ are −2.05, −6.96, −6.98, −8.15, −6.46, −8.15, −5.21, −7.59, −6.21, −7.33, and −7.32 eV, $OsC_4(NH)_4$ has a more negative COHP indicating a strong metal-coordination orbital hybridization. The COHP also

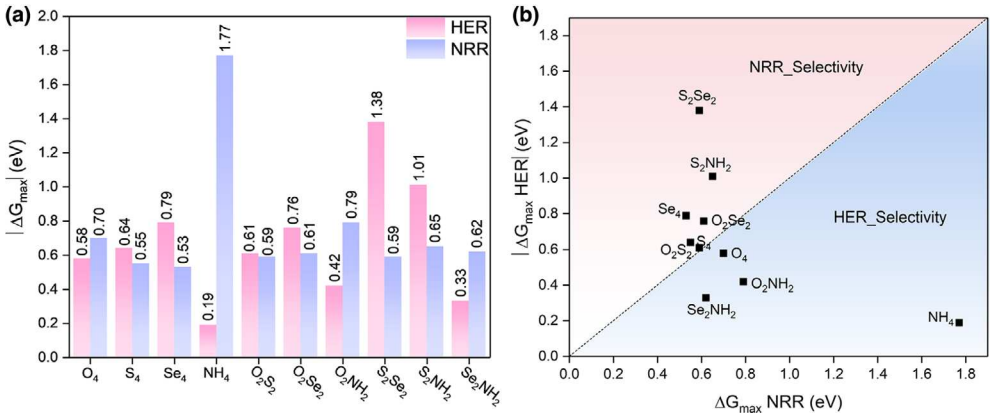

Figure 5. a) The max energy barriers of NRR and HER on OsC_4X_4; b) the selectivity of NRR and HER on OsC_4X_4.

increases with the decrease of Δd-p. This linear correlation gives a quantitative explanation for the role of different metal centers and coordination atoms in determining the bonding/antibonding orbital populations, which is the origin of the observed trends for the adsorption energies of intermediates. This also suggests that our Δd-p can be used as an indicator for the metal-coordination atom bonding strength. A smaller Δd-p would suggest a stronger metal-coordination atom bond, but weaker absorption of the NRR intermediates (Figure S10, Supporting Information). Furthermore, both COHP and ΔE (*N) have a linear relationship with Δd-p (Figure 4d), revealing the reliability of the Δd-p descriptor in revealing the catalytic activity of OsC_4X_4 catalysts.

In order to explore the universality of the conclusions, we further calculated the E_d of M (M = Ir, Ru (that are next to Os element)), E_p of N_2H, and the corresponding ΔG_{max} values of NRR (Tables S8 and S9, Supporting Information). The changing trend between the E_d and ΔG_{max} still has a good linear relationship (Figures S12 and S13, Supporting Information). Then we calculate the Δd-p against the corresponding ΔG_{max}, similarly, there are obvious volcanic relationships between the Δd-p and ΔG_{max}. IrC_4O_4 and $RuC_4(Se)_4$ are located at the apex of the volcanic curve and have the best NRR activity. Therefore, we can conclude that for a specific metal, a proper metal-intermediate atoms p-d orbital hybridization interaction strength is a key indicator for their NRR catalytic activities (Figures S14, Supporting Information).

2.5. Suppression of Hydrogen Evolution Reaction (HER)

Hydrogen evolution reaction (HER) is a competitive reaction of NRR, so we further study the selectivity of NRR and HER on OsC_4X_4. The HER free energies (ΔG(*H)) are shown in Table S10, Supporting Information, and **Figure 5**a. The |ΔG(*H)| of $OsC_4(Se)_4$ is 0.79 eV, which is much higher than the NRR energy barrier (0.53 eV), indicating that it not only has the highest NRR activity but also can inhibit the occurrence of HER. More importantly, a general inverse relationship between the NRR energy barrier (ΔG_{max}) and HER energy barrier (|ΔG(*H)|) is found for OsC_4X_4 (Figure S15a, Supporting Information). For example, as the NRR energy barrier became larger from OsC_4Se_4, OsC_4S_4 to OsC_4O_4, the HER energy barrier gradually became smaller. This further illustrates HER is inhibited by $OsC_4(Se)_4$, while $OsC_4(NH)_4$ may have higher HER activity. The corresponding catalysts in the upper and below regions of Figure 5b are NRR and HER selective, respectively. Similarly, IrC_4O_4 and $RuC_4(Se)_4$ have small NRR energy barriers (0.68 and 0.62 eV) but by large |ΔG(*H)| (2.80 and 1.05 eV), (Tables S11 and S12; Figure S16, Supporting Information). There is also a general inverse relationship between the NRR energy barrier and HER energy barrier (Figure S15b,c, Supporting Information). The NRR is more selective over the $OsC_4(Se)_4$, $RuC_4(Se)_4$, and IrC_4O_4, which are located at the apex of the volcano curve between ΔG_{max} and Δd-p. These data fully proved the inhibitory effect of MC_4X_4 on HER.

3. Conclusions

In this work, the role of individual metal, symmetrical and asymmetrical coordination environment, and the p-d synthetic effect on the electrochemical catalytic performance of NRR on 2DMOFs MC_4X_4 (M = Os, Ru, Ir; X = O, S, Se, NH) nanosheets have been studied based on DFT calculations. The results show that metal atoms are active centers in the NRR process and play a crucial role in the capture and activation of N_2, while the distal mechanism is energetically more favorable for the conversion of N_2 to NH_3. It is also found that the catalytic activity of MC_4X_4 is related to the type of coordinating atoms: for a specific type of metal, a proper metal-intermediate atoms p-d hybridization interaction strength is the key indicator for NRR catalytic activities. The ΔG_{max} and Δd-p have a volcanic relationship with $OsC_4(Se)_4$, IrC_4O_4, $RuC_4(Se)_4$ located at the apex of the volcanic curve and have better NRR performances. The $OsC_4(Se)_4$ shows the best NRR catalytic activity with the lowest overpotential (0.35 V). At the same time, MC_4X_4 can inhibit competing HER and have good selectivity for NRR. Our results systematically proved the application of orbital engineering in electrocatalytic NRR activity, opening an exciting road to the rational design of SACs for advancing sustainable NRR.

4. Experimental Section

Computational Methods: All DFT calculations were performed using the Vienna ab initio simulation package (VASP).[36–38] The Perdew-Burke-Ernzerhof (PBE) function of the Generalized Gradient Approximation (GGA) is used to describe the exchange-correlation energy.[39] To describe the expansion of the electronic eigenfunctions, the projector-augmented wave (PAW) method was applied with a kinetic energy cutoff of 500 eV.[40,41] The total energy and force convergence threshold were set to 10^{-5} eV and 0.02 eV $Å^{-1}$, respectively. The Brillouin zone was sampled with a 4 × 4 × 1 k-point grid of the Monkhorst-Pack scheme.[42] A 15 Å vacuum was set above the nanosheets to avoid interaction between the two periodic images. The van der Waals interactions were considered using the empirical correction via the DFT + D3 scheme.[43,44] Charge density difference and Bader charge analysis were used to describe the charge transfer, the atomic configuration, and charge density difference diagram were shown in the VESTA code.[45,46] Projected crystal orbital Hamilton population (pCOHP) was

calculated using LOBSTER to analyze the interaction between TM atoms and intermediates.[47]

The calculated hydrogen electrode model is used to simulate the electrochemical reaction.[48] The Gibbs free energy change (ΔG) of each elementary step is calculated by the following formula:

$$\Delta G = \Delta E + \Delta E_{ZPE} - T\Delta S + \Delta G_{pH} + \Delta G_U \quad (6)$$

where ΔE is the reaction energy that can be directly obtained by the total energies of DFT. ΔE_{ZPE} and ΔS are the difference in zero-point energy and entropy between the products and the reactants at room temperature (T = 298.15 K), respectively. The difference in zero-point energy could be calculated from the vibration frequency. The entropy and vibrational frequencies of free molecules (such as H_2, N_2, and NH_3) were taken from the NIST database. The effect of the applied electrode potential and pH are contained by the correction of ΔG_U and ΔG_{pH}, respectively.

Acknowledgments

This work was supported by the National Natural Science Foundation of China (21905253, 51973200, and 52122308), the Natural Science Foundation of Henan (202300410372), and the National Supercomputing Center in Zhengzhou.

Conflict of interest

The authors declare no conflict of interest.

Supporting Information

Supporting Information is available from the Wiley Online Library or from the author.

Keywords

first-principle calculations, Nitrogen reduction, p-d orbital hybridization, single-atom catalysts

Received: July 29, 2022
Revised: December 21, 2022
Published online: December 29, 2022

[1] B. H. R. Suryanto, H. Du, D. Wang, J. Chen, A. N. Simonov, *Nat. Catal.* **2019**, *2*, 290.
[2] J. G. Chen, R. M. Crooks, L. C. Seefeldt, K. L. Bren, R. M. Bullock, M. Y. Darensbourg, P. L. Holland, B. Hoffman, M. J. Janik, A. K. Jones, M. G. Kanatzidis, P. King, K. M. Lancaster, S. V. Lymar, P. Pfromm, W. F. Schneider, R. R. Schrock, *Science* **2018**, *360*, eaar6611.
[3] G. Soloveichik, *Nat. Catal.* **2019**, *2*, 377.
[4] V. Kyriakou, I. Garagounis, A. Vourros, E. Vasileiou, M. Stoukides, *Joule* **2020**, *4*, 142.
[5] Y. Fu, T. Li, G. Zhou, J. Guo, Y. Ao, Y. Hu, J. Shen, L. Liu, X. Wu, *Nano Lett.* **2020**, *20*, 4960.
[6] W. Guo, K. Zhang, Z. Liang, R. Zou, Q. Xu, *Chem. Soc. Rev.* **2019**, *48*, 5658.
[7] G. Qing, R. Ghazfar, S. T. Jackowski, F. Habibzadeh, M. M. Ashtiani, C. Chen, M. R. Smith, T. W. Hamann, *Chem. Rev.* **2020**, *120*, 5437.
[8] J. Chen, Y. Kang, W. Zhang, Z. Zhang, Y. Chen, Y. Yang, L. Duan, Y. Li, W. Li, *Angew. Chem. Int. Ed.* **2022**, *61*, e202203022.
[9] L. Han, Z. Ren, P. Ou, H. Cheng, N. Rui, L. Lin, X. Liu, L. Zhuo, J. Song, J. Sun, J. Luo, H. L. Xin, *Angew. Chem. Int. Ed.* **2021**, *60*, 345.
[10] J. Zhao, Z. Chen, *J. Am. Chem. Soc.* **2017**, *139*, 12480.
[11] H. Tao, C. Choi, L. Ding, Z. Jiang, Z. Han, M. Jia, Q. Fan, Y. Gao, H. Wang, A. W. Robertson, S. Hong, Y. Jung, S. Liu, Z. Sun, *Chem* **2019**, *5*, 204.
[12] A. Corma, H. García, F. X. L. i. Xamena, *Chem. Rev.* **2010**, *110*, 4606.
[13] C. A. Downes, S. C. Marinescu, *ChemSusChem* **2017**, *10*, 4374.
[14] K. Ge, S. Sun, Y. Zhao, K. Yang, S. Wang, Z. Zhang, J. Cao, Y. Yang, Y. Zhang, M. Pan, L. Zhu, *Angew. Chem. Int. Ed.* **2021**, *60*, 12097.
[15] H. B. Aiyappa, J. Masa, C. Andronescu, M. Muhler, R. A. Fischer, W. Schuhmann, *Small Methods* **2019**, *3*, 1800415.
[16] L. Jiao, J. Zhu, Y. Zhang, W. Yang, S. Zhou, A. Li, C. Xie, X. Zheng, W. Zhou, S. Yu, H. Jiang, *J. Am. Chem. Soc.* **2021**, *143*, 19417.
[17] Y. Jia, Z. Dr, J. Xue, Q. Yang, J. Liu, Y. Xian, Y. Zhong, X. Sun, Q. Zhang, D. Liu, G. L. Yao, *Angew. Chem. Int. Ed.* **2022**, *61*, e202110838.
[18] D. Micheroni, G. Lan, W. Lin, *J. Am. Chem. Soc.* **2018**, *140*, 15591.
[19] Y. Hao, Q. Liu, Y. Zhou, Z. Yuan, Y. Fan, Z. Ke, C. Su, G. Li, *Energy Environ. Mater.* **2019**, *2*, 18.
[20] R. Zhang, L. Jiao, W. Yang, G. Wan, H. Jiang, *J. Mater. Chem. A* **2019**, *7*, 26371.
[21] T. Kambe, R. Sakamoto, K. Hoshiko, K. Takada, M. Miyachi, J. Ryu, S. Sasaki, J. Kim, K. Nakazato, M. Takata, H. Nishihara, *J. Am. Chem. Soc.* **2013**, *135*, 2462.
[22] H. Liu, X. Li, L. Chen, X. Wang, H. Pan, X. Zhang, M. Zhao, *J. Phys. Chem. C* **2016**, *120*, 3846.
[23] P. Zhang, X. Hou, L. Liu, J. Mi, M. Dong, *J. Phys. Chem. C* **2015**, *119*, 28028.
[24] Y. Ji, H. Dong, C. Liu, Y. Li, *Nanoscale* **2019**, *11*, 454.
[25] X. Liu, Z. Wang, J. Zhao, J. Zhao, Y. Liu, *Appl. Surf. Sci.* **2019**, *487*, 833.
[26] X. Cui, C. Tang, Q. Zhang, *Adv. Energy Mater.* **2018**, *8*, 1800369.
[27] A. Wang, H. Niu, X. Wang, X. Wan, L. Xie, Z. Zhang, J. Wang, Y. Guo, *J. Mater. Chem. A* **2022**, *10*, 13005.
[28] Z. Xue, X. Zhang, J. Qin, R. Liu, *Nano Energy* **2021**, *80*, 105527.
[29] Z. Xue, X. Zhang, J. Qin, R. Liu, *J. Energy Chem.* **2021**, *57*, 443.
[30] S. Back, Y. Jung, *Phys. Chem. Chem. Phys.* **2016**, *18*, 9161.
[31] X. Lv, W. Wei, B. Huang, Y. Dai, T. Frauenheim, *Nano Lett.* **2021**, *21*, 1871.
[32] B. Li, W. Du, Q. Wu, Y. Dai, B. Huang, Y. Ma, *J. Phys. Chem. C* **2021**, *125*, 20870.
[33] B. Hammer, J. K. Nørskov, *Adv. Catal.* **2000**, *45*, 71.
[34] X. Wang, L. Guo, Z. Xie, X. Peng, X. Yu, X. Yang, Z. Lu, X. Zhang, L. Li, *Appl. Surf. Sci.* **2022**, *606*, 154749.
[35] M. A. Hunter, J. M. T. A. Fischer, Q. Yuan, M. Hankel, D. J. Searles, *ACS Catal.* **2019**, *9*, 7660.
[36] G. Kresse, J. Hafner, *Phys. Rev. B* **1993**, *47*, 558.
[37] G. Kresse, J. Hafner, *Phys. Rev. B* **1994**, *49*, 14251.
[38] G. Kresse, J. Furthmüller, *Phys. Rev. B* **1996**, *54*, 11169.
[39] J. P. Perdew, K. Burke, M. Ernzerhof, *Phys. Rev. Lett.* **1996**, *77*, 3865.
[40] P. E. Blöchl, *Phys. Rev. B* **1994**, *50*, 17953.
[41] G. Kresse, D. Joubert, *Phys. Rev. B* **1999**, *59*, 1758.
[42] H. J. Monkhorst, J. D. Pack, *Phys. Rev. B* **1976**, *13*, 5188.
[43] S. Grimme, J. Antony, S. Ehrlich, H. Krieg, *J. Chem. Phys.* **2010**, *132*, 154104.
[44] S. Grimme, S. Ehrlich, L. Goerigk, *J. Comput. Chem.* **2011**, *32*, 1456.
[45] K. Momma, F. Izumi, *J. Appl. Crystallogr.* **2011**, *44*, 1272.
[46] W. Tang, E. Sanville, G. Henkelman, *J. Phys. Condens. Matter* **2009**, *21*, 084204.
[47] R. Nelson, C. Ertural, J. George, V. L. Deringer, G. Hautier, R. Dronskowski, *J. Comput. Chem.* **2020**, *41*, 1931.
[48] J. K. Nørskov, J. Rossmeisl, A. Logadottir, L. Lindqvist, *J. Phys. Chem. B* **2004**, *108*, 17886.